



HAL
open science

Fault-tolerant control allocation for a bio-inspired underactuated AUV in the presence of actuator failures: Design and experiments

Walid Remmas, Ahmed Chemori, Maarja Kruusmaa

► To cite this version:

Walid Remmas, Ahmed Chemori, Maarja Kruusmaa. Fault-tolerant control allocation for a bio-inspired underactuated AUV in the presence of actuator failures: Design and experiments. *Ocean Engineering*, 2023, 285, pp.115327. 10.1016/j.oceaneng.2023.115327 . lirmm-04165240

HAL Id: lirmm-04165240

<https://hal-lirmm.ccsd.cnrs.fr/lirmm-04165240v1>

Submitted on 18 Jul 2023

HAL is a multi-disciplinary open access archive for the deposit and dissemination of scientific research documents, whether they are published or not. The documents may come from teaching and research institutions in France or abroad, or from public or private research centers.

L'archive ouverte pluridisciplinaire **HAL**, est destinée au dépôt et à la diffusion de documents scientifiques de niveau recherche, publiés ou non, émanant des établissements d'enseignement et de recherche français ou étrangers, des laboratoires publics ou privés.

Fault-Tolerant Control Allocation for a Bio-inspired Underactuated AUV in the Presence of Actuator Failures: Design and Experiments.

Walid Remmas^{a,b,*}, Ahmed Chemori^b and Maarja Kruusmaa^a

^aDepartment of Computer Systems, Tallinn University of Technology, Tallinn, Estonia

^bLIRMM, University of Montpellier, CNRS, Montpellier, France

ARTICLE INFO

Keywords:

Fault-tolerance
Fin-actuated robot
Control allocation
Underwater robot
Bio-inspired
Sliding mode control

ABSTRACT

In this paper, we present the mathematical design and implementation of a fault-tolerant control scheme for a bio-inspired underwater robot with four flexible fins. The proposed active fault-tolerant control scheme re-configures the force allocation matrix using the Elimination of Column Method, depending on which fin actuator is faulty. The proposed method allows to decouple the 6-DOF controllable underwater vehicle using the remaining three fins. The efficacy of the proposed method is assessed experimentally for trajectory tracking of an ellipsoidal-shaped trajectory using two different controllers, namely PID control and Sliding Mode control. The obtained results show that the combination of a sliding mode controller with the proposed fault-tolerant control allocation approach ensures an efficient trajectory tracking control performance when faults occur.

1. Introduction

Autonomous Underwater Vehicles (AUVs) are often deployed in challenging environments, where they should function reliably even in the presence of components' failures. Fault-tolerant Control (FTC) for underwater robots is of high importance, as it ensures a more robust and reliable autonomy, and reduces the risk of losing the vehicle during its mission.

The development of effective fault-tolerant control strategies for thruster-based underwater robots has been an active area of research in recent years Antonelli (2003); Liu, Tang, Qin, Duan, Luo and Pu (2022a). Researchers have explored a range of techniques, dealing with the three main components of FTC: (i) fault detection, (ii) fault isolation, and (iii) fault accommodation. Fault detection involves recognizing when a failure has occurred that prevents the vehicle from operating correctly. Fault isolation involves identifying the cause of the failure and its location. Fault detection and isolation have been studied extensively, and the reader can refer to Antonelli (2003); Samy, Postlethwaite and Gu (2011); Liu et al. (2022a) and the references therein. Finally, fault accommodation, which is investigated in this work, involves controlling the vehicle to execute a desired task in the presence of a failure.

Fault accommodation has been addressed in the literature using two main approaches, namely active and passive FTC. Active fault-tolerant control, such as control reconfiguration Ni (2001); Sarkar, Podder and Antonelli (2002) and control allocation Omerdic and Roberts (2004); Alwi and Edwards (2008); Baldini, Ciabattone, Felicetti, Ferracuti, Monteriù, Fasano and Freddi (2017), involves continuously

This work was supported by ROBOTURTLE KIM Sea & Coast Research project.

*Corresponding author

✉ walid.remmas@taltech.ee (W. Remmas); ahmed.chemori@lirmm.fr (A. Chemori); maarja.kruusmaa@taltech.ee (M. Kruusmaa)
ORCID(s): 0000-0001-8690-0496 (W. Remmas); 0000-0001-9739-9473 (A. Chemori); 0000-0001-5738-5421 (M. Kruusmaa)

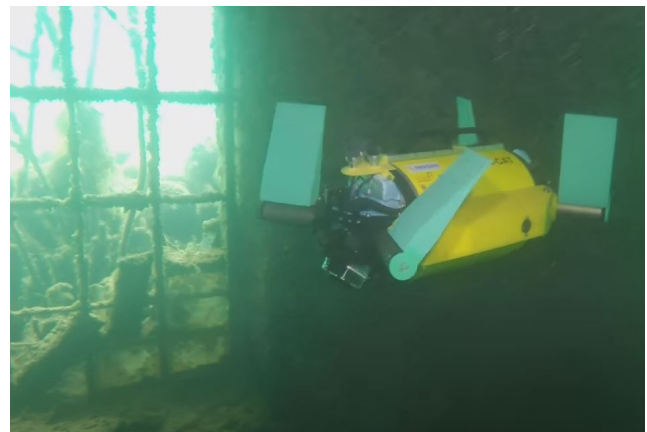


Figure 1: View of U-CAT robot during an inspection mission in a submerged structure.

monitoring the system for potential failures and implementing corrective measures to prevent or mitigate the effects of any hardware failures. Passive fault-tolerant control Liu, Zhang, Liu and Zhao (2022b); Wang, Wilson, Liu et al. (2015), on the other hand, relies on the inherent redundancy and robustness of the system design to tolerate failures and continue operating without the need for active monitoring or intervention.

Most of the above-mentioned studies have focused on thruster-actuated designs of AUVs. However, fin-actuated AUVs have garnered significant attention RB, Hemakumar and Prasad (2018); Scaradozzi, Palmieri, Costa and Pinelli (2017), due to their improved locomotion efficiency Yu and Wang (2005) and maneuverability Weymouth (2016). Despite this, the topic of fault-tolerant control for fin-actuated AUVs has received little attention in the literature. As far as the authors are aware, the only work on fault-tolerant control for a bio-inspired robot was published in Yang, Wang, Wu and Yu (2018). The authors in Yang et al. (2018) proposed a passive FTC scheme using a central pattern generator based

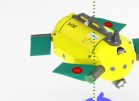
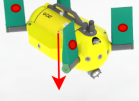
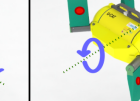
	Surge	Sway	Heave	Roll	Pitch	Yaw
2 Fins						
4 Fins						

Figure 2: Illustration of the various fin configurations allowing to control the robot in each DOF using either 2 or 4 fins. The actuated fins for each configuration are highlighted with a red dot.

controller to correct the heading of fish-like robot with a multi-joint tail design.

This paper focuses on active fault-tolerant control of a four fin-actuated AUV in the presence of actuator failures. A control allocation switching mechanism is proposed to accurately re-distribute the fins' forces when a failure occurs. The proposed FTC method is based on the column elimination method Yang, Yuh and Choi (1998); Kadiyam, Parashar, Mohan and Deshmukh (2020), which is adapted and applied to the specific challenges posed by the highly coupled and highly nonlinear fin-based actuation system. The proposed FTC scheme has been experimentally evaluated for controlling three degrees of freedom, using two different controllers: PID control and Sliding mode control. The main contributions of this paper are as follows:

- The development and application of FTC scheme for fin-actuated AUVs, which considers the unique challenges of highly coupled and highly nonlinear fin-based actuation systems.
- The experimental assessment of the proposed FTC scheme in controlling three degrees of freedom, using both PID and Sliding mode controllers.
- A comprehensive experimental analysis is provided, including multiple scenarios to assess the robustness and adaptability of the proposed FTC scheme.
- The work highlights the challenges and complexities of implementing fault-tolerant control on a highly coupled, under-actuated AUV, and discusses potential directions for future research in this area.
- The paper contributes to the understanding of how control allocation switching mechanisms can be employed effectively for fin-actuated AUVs, and can potentially serve as a foundation for future studies on fault-tolerant control for similar systems.
- To the best of the authors' knowledge, the presented work is the first one dealing with active fault-tolerant control of fin-actuated underwater robots.

The remainder of the paper is organized in the following manner: Section 2 provides a detailed description of the fin-actuated autonomous underwater vehicle (AUV) and its dynamic model, and outlines the problem of control allocation for such systems. In Section 3, we present our proposed fault-tolerant control solution and the corresponding control laws that have been implemented. Section 4 presents the experimental setup, including the various scenarios that were studied, and presents the obtained results. Finally, we offer some concluding remarks and suggest potential directions for future work in Section 5.

2. Background and Problem Formulation

This section begins by presenting the fin-actuated AUV U-CAT, as well as its hydro-dynamic model. We also presents the problem formulation, which outlines the specific problem that the proposed FTC scheme aims to solve.

2.1. U-CAT biomimetic AUV

U-CAT is a biomimetic underwater vehicle able to easily move and maneuver along six degrees of freedom using its four flexible fins Salumäe, Raag, Rebane, Ernits,

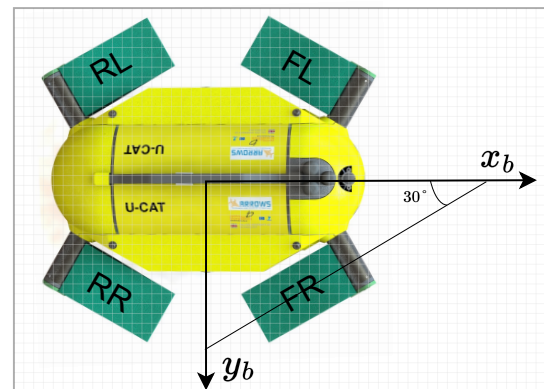


Figure 3: Illustration of U-CAT's fins configuration. The robot front right, rear right, rear left, and front left are denoted by FR, RR, RL, and FL, respectively.

Toming, Ratas and Kruusmaa (2014). It was designed for the inspection of confined environments such as shipwrecks and underwater structures autonomously or semi-autonomously. It was used in previous works for various applications, such as vision-based navigation Preston, Salumäe and Kruusmaa (2018), validation of control schemes for fin-actuated vehicles Chemori, Kuusmik, Salumäe and Kruusmaa (2016); Meurer, Simha, Kotta and Kruusmaa (2019); Remmas, Chemori and Kruusmaa (2021a); Salumäe, Chemori and Kruusmaa (2016); Salumäe, Chemori and Kruusmaa (2019), and study of fish/robot interaction Kruusmaa, Gkliva, Tuh-tan, Tuvikene and Alfredsen (2020). Further technical details about U-CAT can be found in Remmas, Chemori and Kruusmaa (2021b).

2.2. AUV Dynamic model

This subsection describes the kinematic and dynamic models of the AUV, moving in six degrees of freedom. It can be expressed, following Fossen's notation, as Fossen (2011):

$$\begin{aligned} \dot{\eta} &= J(q)v \\ M\dot{v} + n(\eta, v) &= \tau \\ n(\eta, v) &= C(v)v + D(v)v + g(\eta) \end{aligned} \quad (1)$$

Where $\eta = [x, y, z, \Phi, \theta, \psi]^T \in \mathbb{R}^6$ represents the vector of the vehicle's position and orientation in the earth-fixed frame R_n , and $v = [u, v, w, p, q, r]^T \in \mathbb{R}^6$ represents the vector of linear and angular velocities in the body-fixed frame R_b . The matrix $M \in \mathbb{R}^{6 \times 6}$ is the mass matrix of the robot, $C(v) \in \mathbb{R}^{6 \times 6}$ denotes the Coriolis and centripetal matrix, $D(v) \in \mathbb{R}^{6 \times 6}$ is the hydrodynamic damping matrix, and $g(\eta) \in \mathbb{R}^6$ denotes the restoring forces and moments due to buoyancy and gravity. The generalized forces and moments on the vehicle, expressed in the body-fixed frame, are represented by $\tau = [\tau_x, \tau_y, \tau_z, \tau_\Phi, \tau_\theta, \tau_\psi]^T$.

The Jacobian $J(\eta)$ is expressed, using the Euler angles notation, to map the velocities expressed in R_b to the earth-fixed frame R_n such that:

$$J(\eta) = \begin{bmatrix} R(\eta) & 0_{3 \times 3} \\ 0_{3 \times 3} & T(\eta) \end{bmatrix} \quad (2)$$

with its inverse as follows:

$$J(\eta)^{-1} = \begin{bmatrix} R(\eta)^T & 0_{3 \times 3} \\ 0_{3 \times 3} & T(\eta)^T \end{bmatrix} \quad (3)$$

where the matrices $R(\eta)$ and $T(\eta)$ are defined as:

$$R(\eta) = \begin{bmatrix} c\psi c\theta & -s\psi c\Phi + c\psi s\theta s\Phi & s\psi s\Phi + c\psi s\theta s\Phi \\ s\psi c\theta & c\psi c\Phi + s\psi s\theta s\Phi & -c\psi s\Phi + s\psi s\theta c\Phi \\ -c\theta & c\theta s\Phi & c\theta c\Phi \end{bmatrix}$$

$$T(\eta) = \begin{bmatrix} 1 & s\Phi t\theta & c\Phi t\theta \\ 0 & c\Phi & -s\Phi \\ 0 & \frac{s\Phi}{c\theta} & \frac{c\Phi}{c\theta} \end{bmatrix}$$

with $c. = \cos(.)$, $s. = \sin(.)$, and $t. = \tan(.)$.

2.3. Problem formulation of Control allocation

Fin-actuated AUV's can achieve locomotion by moving their fins with an oscillatory profile Low (2011). For the motion control of U-CAT AUV, we propose to use the following oscillatory profile:

$$\varphi_i(t) = A_i \sin(\omega t) + \phi_i \quad i = 1 \dots 4 \quad (4)$$

Where $\varphi_i(t)$ is the instantaneous angle of each fin i , A_i denotes the oscillating amplitude, ω the oscillating frequency, and ϕ_i the zero-direction angle. The indices $i = \{1, 2, 3, 4\}$ are allocated for the Front Right (FR), Rear Right (RR), Rear Left (RL), and Front Left (FL) fins, respectively.

When a fin is oscillating, we assume that it generates a constant thrust force f_i along the zero-direction angle ϕ_i , which is the mean thrust force generated from one flapping cycle Ren, Wang and Wen (2015); Xie, Zhu, Shen and Ren (2018). The generated fin forces can then be mapped to body-frame wrench τ using the following nonlinear model:

$$\begin{aligned} \tau_x &= c\psi_f (c\phi_1 f_1 - c\phi_2 f_2 - c\phi_3 f_3 + c\phi_4 f_4) \\ \tau_y &= s\psi_f (-c\phi_1 f_1 - c\phi_2 f_2 + c\phi_3 f_3 + c\phi_4 f_4) \\ \tau_z &= s\phi_1 f_1 + s\phi_2 f_2 + s\phi_3 f_3 + s\phi_4 f_4 \\ \tau_\Phi &= M_\Phi (s\phi_1 f_1 + s\phi_2 f_2 - s\phi_3 f_3 - s\phi_4 f_4) \\ \tau_\theta &= M_\theta (-s\phi_1 f_1 + s\phi_2 f_2 + s\phi_3 f_3 - s\phi_4 f_4) \\ \tau_\psi &= M_\psi (-c\phi_1 f_1 + c\phi_2 f_2 - c\phi_3 f_3 + c\phi_4 f_4) \end{aligned} \quad (5)$$

The constant $\psi_f = 30^\circ = 0.52 \text{ rad}$, denotes the fin orientation angle in the body frame as illustrated in Fig. 3, and the constants $M_\Phi = 0.15$, $M_\theta = 0.26$, and $M_\psi = 0.29$, denote the moment arm values along roll, pitch, and yaw axes, respectively.

The equation system described in (5) can be rewritten in a compact matricial form as $B[H_c, V_c]^T = \tau_n$, equivalent to:

$$\begin{bmatrix} C_h^1 & C_h^2 & C_h^3 & C_h^4 & C_v^1 & C_v^2 & C_v^3 & C_v^4 \\ 1 & -1 & -1 & 1 & 0 & 0 & 0 & 0 \\ -1 & -1 & 1 & 1 & 0 & 0 & 0 & 0 \\ 0 & 0 & 0 & 0 & 1 & 1 & 1 & 1 \\ 0 & 0 & 0 & 0 & 1 & 1 & -1 & -1 \\ 0 & 0 & 0 & 0 & -1 & 1 & 1 & -1 \\ -1 & 1 & -1 & 1 & 0 & 0 & 0 & 0 \end{bmatrix} \begin{bmatrix} H_c \\ V_c \end{bmatrix} = \tau_n \quad (6)$$

With $\tau_n = [\frac{\tau_x}{c\psi_f}, \frac{\tau_y}{s\psi_f}, \tau_z, \frac{\tau_\Phi}{M_\Phi}, \frac{\tau_\theta}{M_\theta}, \frac{\tau_\psi}{M_\psi}]^T$. The two vectors $H_c = [c\phi_1 f_1, c\phi_2 f_2, c\phi_3 f_3, c\phi_4 f_4]^T$ and $V_c = [s\phi_1 f_1, s\phi_2 f_2, s\phi_3 f_3, s\phi_4 f_4]^T$ denote the generated thrust forces, projected on the horizontal and vertical planes of the body-fixed frame, respectively. The symbols C_h^i and C_v^i (for $i = 1 \dots 4$) are used as labels for the columns of the allocation matrix.

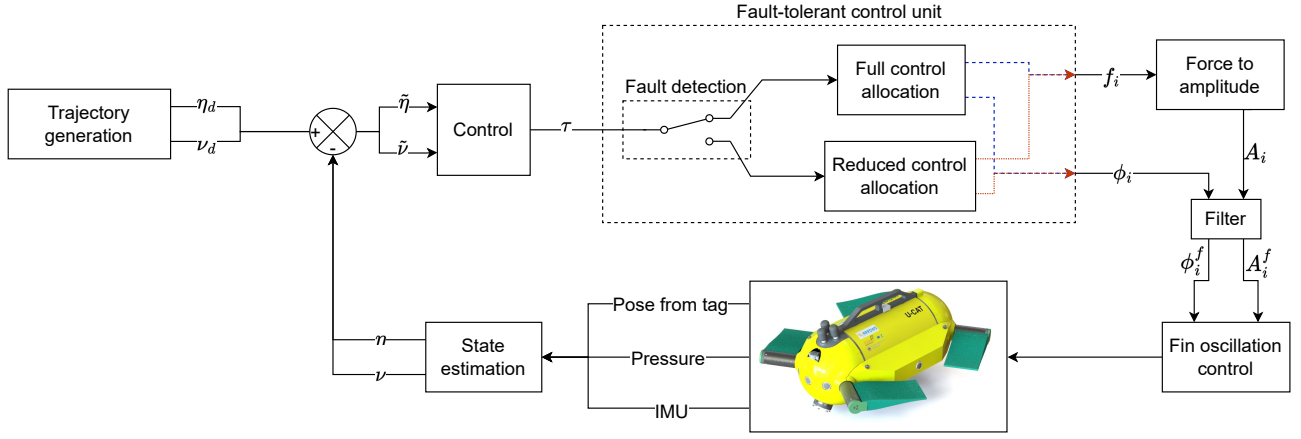


Figure 4: Block Diagram illustration of the proposed fault-tolerant control strategy.

3. Proposed Fault Tolerant Control Unit

Before describing the proposed fault-tolerant control scheme (cf. Fig. 4), let us introduce the detailed steps to solve the control-allocation problem in the nominal case, i.e. where all fins are fully functional. The control allocation problem was solved in previous works following an empirical approach Salumäe et al. (2016). In this study we present an analytical solution that solves the linear algebraic set of equations, presented in (6). The system is considered to be virtually over-actuated, since the fins have an infinite number of possible configurations. The simplest and straightforward solution would be to take directly the Moore-Penrose inverse Penrose (1955), such that $[H_c, V_c]^T = B^\dagger \tau_n$. Where $B^\dagger = B^T(BB^T)^{-1}$ results in the following:

$$B^\dagger = \frac{1}{4} \begin{bmatrix} 1 & -1 & 0 & 0 & 0 & -1 \\ -1 & -1 & 0 & 0 & 0 & 1 \\ -1 & 1 & 0 & 0 & 0 & -1 \\ 1 & 1 & 0 & 0 & 0 & 1 \\ 0 & 0 & 1 & 1 & -1 & 0 \\ 0 & 0 & 1 & 1 & 1 & 0 \\ 0 & 0 & 1 & -1 & 1 & 0 \\ 0 & 0 & 1 & -1 & -1 & 0 \end{bmatrix} \quad (7)$$

This leads to the following solution where the fins' forces and orientations are still coupled:

$$c\phi_1 f_1 = \frac{1}{4} \left(\frac{\tau_x}{c\psi_f} - \frac{\tau_y}{s\psi_f} - \frac{\tau_\psi}{M_\psi} \right) \quad (8)$$

$$c\phi_2 f_2 = \frac{1}{4} \left(-\frac{\tau_x}{c\psi_f} - \frac{\tau_y}{s\psi_f} + \frac{\tau_\psi}{M_\psi} \right) \quad (9)$$

$$c\phi_3 f_3 = \frac{1}{4} \left(-\frac{\tau_x}{c\psi_f} + \frac{\tau_y}{s\psi_f} - \frac{\tau_\psi}{M_\psi} \right) \quad (10)$$

$$c\phi_4 f_4 = \frac{1}{4} \left(\frac{\tau_x}{c\psi_f} + \frac{\tau_y}{s\psi_f} + \frac{\tau_\psi}{M_\psi} \right) \quad (11)$$

$$s\phi_1 f_1 = \frac{1}{4} \left(\tau_z + \frac{\tau_\Phi}{M_\Phi} - \frac{\tau_\Theta}{M_\Theta} \right) \quad (12)$$

$$s\phi_2 f_2 = \frac{1}{4} \left(\tau_z + \frac{\tau_\Phi}{M_\Phi} + \frac{\tau_\Theta}{M_\Theta} \right) \quad (13)$$

$$s\phi_3 f_3 = \frac{1}{4} \left(\tau_z - \frac{\tau_\Phi}{M_\Phi} + \frac{\tau_\Theta}{M_\Theta} \right) \quad (14)$$

$$s\phi_4 f_4 = \frac{1}{4} \left(\tau_z - \frac{\tau_\Phi}{M_\Phi} - \frac{\tau_\Theta}{M_\Theta} \right) \quad (15)$$

By dividing equations (12) (13) (14) (15) by equations (8) (9) (10) (11), respectively, we can deduce the zero-direction angles ϕ_1 , ϕ_2 , ϕ_3 and ϕ_4 as follows:

$$\phi_1 = \text{atan} \left(\frac{\tau_z + \frac{\tau_\Phi}{M_\Phi} - \frac{\tau_\Theta}{M_\Theta}}{\frac{\tau_x}{c\psi_f} - \frac{\tau_y}{s\psi_f} - \frac{\tau_\psi}{M_\psi}} \right) \quad (16)$$

$$\phi_2 = \text{atan} \left(\frac{\tau_z + \frac{\tau_\Phi}{M_\Phi} + \frac{\tau_\Theta}{M_\Theta}}{\frac{-\tau_x}{c\psi_f} - \frac{\tau_y}{s\psi_f} + \frac{\tau_\psi}{M_\psi}} \right) \quad (17)$$

$$\phi_3 = \text{atan} \left(\frac{\tau_z - \frac{\tau_\Phi}{M_\Phi} + \frac{\tau_\Theta}{M_\Theta}}{\frac{-\tau_x}{c\psi_f} + \frac{\tau_y}{s\psi_f} - \frac{\tau_\psi}{M_\psi}} \right) \quad (18)$$

$$\phi_4 = \text{atan} \left(\frac{\tau_z - \frac{\tau_\Phi}{M_\Phi} - \frac{\tau_\Theta}{M_\Theta}}{\frac{\tau_x}{c\psi_f} + \frac{\tau_y}{s\psi_f} + \frac{\tau_\psi}{M_\psi}} \right) \quad (19)$$

The fins' forces f_1 , f_2 , f_3 and f_4 are derived by respectively summing and squaring the equations (8) and (12), (9) and (13), (10) and (14), and finally (11) and (15), which leads to the following expressions:

$$f_1 = \frac{1}{4} \sqrt{\left(\frac{\tau_x}{c\psi_f} - \frac{\tau_y}{s\psi_f} - \frac{\tau_\psi}{M_\psi} \right)^2 + \left(\tau_z + \frac{\tau_\Phi}{M_\Phi} - \frac{\tau_\Theta}{M_\Theta} \right)^2} \quad (20)$$

$$f_2 = \frac{1}{4} \sqrt{\left(-\frac{\tau_x}{c\psi_f} - \frac{\tau_y}{s\psi_f} + \frac{\tau_\psi}{M_\psi} \right)^2 + \left(\tau_z + \frac{\tau_\Phi}{M_\Phi} + \frac{\tau_\Theta}{M_\Theta} \right)^2} \quad (21)$$

$$f_3 = \frac{1}{4} \sqrt{\left(\frac{-\tau_x}{c\psi_f} + \frac{\tau_y}{s\psi_f} - \frac{\tau_\psi}{M_\psi}\right)^2 + \left(\tau_z - \frac{\tau_\Phi}{M_\Phi} + \frac{\tau_\Theta}{M_\Theta}\right)^2} \quad (22)$$

$$f_4 = \frac{1}{4} \sqrt{\left(\frac{\tau_x}{c\psi_f} + \frac{\tau_y}{s\psi_f} + \frac{\tau_\psi}{M_\psi}\right)^2 + \left(\tau_z - \frac{\tau_\Phi}{M_\Phi} - \frac{\tau_\Theta}{M_\Theta}\right)^2} \quad (23)$$

The derived solution presented above for controlling the fins' orientations and thrust forces is not optimal for accurately tracking time-varying trajectories, since all the four fins need to be actuated regardless of the control input τ . This may cause for instance the four fins to rotate 180 degrees when the surge component changes its sign. To tackle this issue, we propose to take advantage of the symmetrical configuration of U-CAT fins. Indeed, for forces and torques produced in the horizontal plane of the body-fixed frame such as surge, sway and yaw, only two fins can be used to move in one direction, as illustrated in Fig. 2. We can consequently reformulate the control allocation as follows:

$$\phi_1 = \text{atan} \left(\frac{\tau_z + \frac{\tau_\Phi}{M_\Phi} - \frac{\tau_\Theta}{M_\Theta}}{2 \left(\frac{H(\tau_x)\tau_x}{c\psi_f} - \frac{H(-\tau_y)\tau_y}{s\psi_f} - \frac{H(-\tau_\psi)\tau_\psi}{M_\psi} \right)} \right) \quad (24)$$

$$\phi_2 = \text{atan} \left(\frac{\tau_z + \frac{\tau_\Phi}{M_\Phi} + \frac{\tau_\Theta}{M_\Theta}}{2 \left(-\frac{H(-\tau_x)\tau_x}{c\psi_f} - \frac{H(-\tau_y)\tau_y}{s\psi_f} + \frac{H(\tau_\psi)\tau_\psi}{M_\psi} \right)} \right) \quad (25)$$

$$\phi_3 = \text{atan} \left(\frac{\tau_z - \frac{\tau_\Phi}{M_\Phi} + \frac{\tau_\Theta}{M_\Theta}}{2 \left(-\frac{H(-\tau_x)\tau_x}{c\psi_f} + \frac{H(\tau_y)\tau_y}{s\psi_f} - \frac{H(-\tau_\psi)\tau_\psi}{M_\psi} \right)} \right) \quad (26)$$

$$\phi_4 = \text{atan} \left(\frac{\tau_z - \frac{\tau_\Phi}{M_\Phi} - \frac{\tau_\Theta}{M_\Theta}}{2 \left(\frac{H(\tau_x)\tau_x}{c\psi_f} + \frac{H(\tau_y)\tau_y}{s\psi_f} + \frac{H(\tau_\psi)\tau_\psi}{M_\psi} \right)} \right) \quad (27)$$

$$f_1 = \frac{1}{4} \left[2 \left(\frac{H(\tau_x)\tau_x}{c\psi_f} + \frac{-H(-\tau_y)\tau_y}{s\psi_f} + \frac{-H(-\tau_\psi)\tau_\psi}{M_\psi} \right)^2 + \left(\tau_z + \frac{\tau_\Phi}{M_\Phi} - \frac{\tau_\Theta}{M_\Theta} \right)^2 \right]^{\frac{1}{2}} \quad (28)$$

$$f_2 = \frac{1}{4} \left[2 \left(\frac{-H(-\tau_x)\tau_x}{c\psi_f} + \frac{-H(-\tau_y)\tau_y}{s\psi_f} + \frac{H(\tau_\psi)\tau_\psi}{M_\psi} \right)^2 + \left(\tau_z + \frac{\tau_\Phi}{M_\Phi} + \frac{\tau_\Theta}{M_\Theta} \right)^2 \right]^{\frac{1}{2}} \quad (29)$$

$$f_3 = \frac{1}{4} \left[2 \left(\frac{-H(-\tau_x)\tau_x}{c\psi_f} + \frac{H(\tau_y)\tau_y}{s\psi_f} + \frac{-H(-\tau_\psi)\tau_\psi}{M_\psi} \right)^2 + \left(\tau_z - \frac{\tau_\Phi}{M_\Phi} + \frac{\tau_\Theta}{M_\Theta} \right)^2 \right]^{\frac{1}{2}} \quad (30)$$

$$f_4 = \frac{1}{4} \left[2 \left(\frac{H(\tau_x)\tau_x}{c\psi_f} + \frac{H(\tau_y)\tau_y}{s\psi_f} + \frac{H(\tau_\psi)\tau_\psi}{M_\psi} \right)^2 + \left(\tau_z - \frac{\tau_\Phi}{M_\Phi} - \frac{\tau_\Theta}{M_\Theta} \right)^2 \right]^{\frac{1}{2}} \quad (31)$$

Once the required force for each fin is computed, it should be converted to a fin-oscillating amplitude using

Table 1

Parametric values of the force to amplitude model (32).

ρ (kg/m ³)	S_f (m ²)	ω (rad/s)	r_c (m)	C_d
997	0.02	4π	0.1	0.23

the inverse model described in Remmas et al. (2021b) as follows:

$$A_i = \arccos \left(\frac{-f_i}{2C_d\rho S_f(r_c\omega)^2} + 1 \right) \quad (32)$$

where ω denotes the angular velocity of the fin, ρ is the water density, r_c is the distance between the rotation axis and the center of gravity of the fin, S_f is the projection area of the fin, and C_d stands for the drag coefficient. The drag coefficient C_d was identified experimentally in our previous work Remmas et al. (2021b). The above mentioned parameters are summarized in Table 1.

The resulting amplitudes A_i and zero-directions ϕ_i are then filtered using a second order filter. This is to ensure smooth and continuous transitions, which may significantly reduce the effect of the non-modelled fin lateral forces. The expressions of the used filters are as follows:

$$\ddot{A}_i^f + 2\gamma_A \dot{A}_i^f + \gamma_A^2 (A_i^f - A_i) = 0 \quad (33)$$

$$\ddot{\phi}_i^f + 2\gamma_\phi \dot{\phi}_i^f + \gamma_\phi^2 (\phi_i^f - \phi_i) = 0 \quad (34)$$

Where $\gamma_A = 10$ and $\gamma_\phi = 3$ are positive constants. The values of ϕ_i^f and A_i^f are computed using Euler's integration method, with a step-size of 0.01s, and are then sent to the low-level control of the fins' motors to achieve the desired oscillation profile.

3.1. Control-allocation based FTC

An actuation fault may occur due to various reasons, it can be of mechanical or electrical cause. In both cases, one or several fins may become either malfunctioning, or totally fail to function. In this study, we consider the case of fin failure, and assume that the fault can be identified and isolated. We also assume that only one actuator failure occurs at a time. Throughout the remainder of this paper, when referring to a fin as "faulty," it implies that the fin is completely nonfunctional.

When an actuation failure occurs. We use the elimination of column method to adapt the control allocation system. The matrix B reported in equation (6) is then reduced by two columns depending on which fin is faulty (cf. illustration of Fig. 3). The two following columns are eliminated depending on which fin is faulty:

- C_h^1 and C_v^1 , when the fin *FR* is faulty
- C_h^2 and C_v^2 , when the fin *RR* is faulty
- C_h^3 and C_v^3 , when the fin *RL* is faulty

Table 2
Numerical values of B_r^{-1} for all possible faulty fin cases.

FR		RR	
$\frac{1}{2}$	$\begin{bmatrix} -1 & 0 & 0 & 0 & 0 & 1 \\ -1 & 1 & 0 & 0 & 0 & 0 \\ 0 & 1 & 0 & 0 & 0 & 1 \\ 0 & 0 & 1 & 1 & 0 & 0 \\ 0 & 0 & 0 & -1 & 1 & 0 \\ 0 & 0 & 1 & 0 & -1 & 0 \end{bmatrix}$	$\frac{1}{2}$	$\begin{bmatrix} 1 & 0 & 0 & 0 & 0 & -1 \\ 0 & 1 & 0 & 0 & 0 & -1 \\ 1 & 1 & 0 & 0 & 0 & 0 \\ 0 & 0 & 1 & 1 & 0 & 0 \\ 0 & 0 & 1 & 0 & 1 & 0 \\ 0 & 0 & 0 & -1 & -1 & 0 \end{bmatrix}$
FL		RL	
$\frac{1}{2}$	$\begin{bmatrix} 0 & -1 & 0 & 0 & 0 & -1 \\ -1 & -1 & 0 & 0 & 0 & 0 \\ -1 & 0 & 0 & 0 & 0 & -1 \\ 0 & 0 & 1 & 0 & -1 & 0 \\ 0 & 0 & 0 & 1 & 1 & 0 \\ 0 & 0 & 1 & -1 & 0 & 0 \end{bmatrix}$	$\frac{1}{2}$	$\begin{bmatrix} 1 & -1 & 0 & 0 & 0 & 0 \\ 0 & -1 & 0 & 0 & 0 & 1 \\ 1 & 0 & 0 & 0 & 0 & 1 \\ 0 & 0 & 0 & 1 & -1 & 0 \\ 0 & 0 & 1 & 0 & 1 & 0 \\ 0 & 0 & 1 & -1 & 0 & 0 \end{bmatrix}$

- C_h^4 and C_v^4 , when the fin FL is faulty

Once the two columns are identified and eliminated, the reduced matrix denoted by $A_r \in \mathbb{R}^{6 \times 6}$ becomes a full rank square matrix. This means that, in the case of a faulty fin scenario, A_r is invertible, and there exists only one fin configuration that solves the control allocation problem. Moreover, its inverse A_r^{-1} can be generalized to all the faulty cases listed above, as follows:

$$B_r^{-1} = \begin{bmatrix} H^1 & H^2 & 0 & 0 & 0 & V^1 \\ H^1 & H^2 & 0 & 0 & 0 & V^1 \\ H^2 & H^2 & 0 & 0 & 0 & V^2 \\ H^3 & H^3 & 0 & 0 & 0 & V^3 \\ 0 & 0 & H^4 & V^4 & V^2 & 0 \\ 0 & 0 & H^5 & V^5 & V^2 & 0 \\ 0 & 0 & H^6 & V^6 & V^2 & 0 \end{bmatrix} \quad (35)$$

The resulting values of the B_r^{-1} for all faulty fin cases are summarized in Table 2.

Following the same solving procedure detailed in equations (8) to (23), we can deduce both the required forces and zero-direction angles required for the three healthy fins, as follows:

$$f_i \cos(\phi_i) = H_i^1 \frac{\tau_x}{c\psi_f} + H_i^2 \frac{\tau_y}{s\psi_f} + V_i^1 \frac{\tau_\psi}{M_\psi} = \Gamma_i^h \quad (i = 1 \dots 3) \quad (36)$$

$$f_i \sin(\phi_i) = H_{i+3}^1 \tau_z + V_{i+3}^1 \frac{\tau_\Phi}{M_\Phi} + V_{i+3}^2 \frac{\tau_\theta}{M_\theta} = \Gamma_i^v \quad (i = 1 \dots 3) \quad (37)$$

The required zero-direction angles and forces are then derived and expressed as:

$$f_i = \sqrt{\Gamma_i^{h^2} + \Gamma_i^{v^2}} \quad (i = 1 \dots 3) \quad (38)$$

$$\phi_i = \text{atan}\left(\frac{\Gamma_i^v}{\Gamma_i^h}\right) \quad (i = 1 \dots 3) \quad (39)$$

The computed forces f_i are then transformed into fin oscillation amplitudes A_i using (32). Finally A_i and ϕ_i are filtered using (33) and (34).

The resulting fin oscillating amplitudes A_i^f and zero-direction angles ϕ_i^f are allocated to the respective fins in an ascending order of i as follows:

- RR, RL and FL, when the FR fin is faulty.
- FR, RL, and FL, when the RR fin is faulty.
- FR, RR, and FL, when the RL fin is faulty.
- FR, RR and RL, when the FL fin is faulty.

It is important to note that during the transition from one control allocation matrix to another one leads to varying fin oscillation parameters. This primarily results in different commanded zero-directions and amplitudes for the fins, generating a finite amount of non-modelled external disturbance during rotation, which can be managed by selecting suitable control parameters. Moreover, the coefficients γ_A and γ_{phi} of the second-order filters, as indicated in equations (33) and (34), have been manually adjusted to ensure smooth transitions with minimal external disturbance during changes in fin zero-direction angles.

3.2. Implemented controllers

To study the performance of the proposed FTC scheme for trajectory tracking, we implemented two controllers, namely a PID and a Sliding Mode controller. Let us define the tracking error and its derivative as follows:

$$\tilde{\eta} = \eta_d - \eta \quad (40)$$

$$\tilde{v} = J^{-1} \dot{\eta}_d - v \quad (41)$$

3.2.1. PID Control

A conventional PID controller was implemented as a base-line control law to assess the performance in terms of trajectory tracking using the proposed FTC scheme. There are several variants of PID controllers for AUVs control Fossen (2011). In this study we adopt the model-free one, as we do not have a high confidence in values of the hydrodynamic parameters of the model defined in (1). The control input is expressed as:

$$\tau_{PID} = K_p \tilde{\eta} + K_d \tilde{v} + K_i \int_0^{t_1} \tilde{\eta}(t) dt \quad (42)$$

Where the $K_p \in \mathbb{R}^{6 \times 6}$, $K_d \in \mathbb{R}^{6 \times 6}$ and $K_i \in \mathbb{R}^{6 \times 6}$ are diagonal positive-definite matrices.

3.2.2. Sliding mode Control

In addressing the necessity for robustness against uncertain parameters in the model, we propose the implementation of a Sliding Mode (SM) controller. SM control is widely recognized for its superior performance in managing system uncertainties, disturbances, and nonlinearities, as compared to traditional PID control methods. The design methodology

of the SM controller yields a closed-loop system exhibiting insensitivity to both disturbances and uncertainties Utkin (2013); Slotine, Li et al. (1991). A comprehensive body of research exists on Sliding Mode control in the literature Gambhire, Kishore, Londhe and Pawar (2021). In this study, we focus on the design and implementation of a first-order SM controller. To do so, we define first the sliding surface $s = \dot{v} + \alpha\tilde{\eta}$. Where α is a 6×6 diagonal matrix with positive coefficients. We consider then the positive-definite Lyapunov function $V = \frac{1}{2}s^2$. To ensure asymptotic stability, the control law should ensure $\dot{V} < 0$ Edwards and Spurgeon (1998). Which leads to the following control law:

$$\tau = n(\eta, v) + M(J^{-1}\ddot{\eta}_d + \dot{J}^{-1}\dot{\eta}_d + \alpha(\dot{\eta}_d - \dot{\eta}) + K \text{sign}(s)) \quad (43)$$

To avoid the chattering phenomena, inherent to first-order SM, and caused by the $\text{sign}()$ function, we propose to use a hyperbolic tangent function instead. The resulting control law becomes:

$$\tau_{SM} = n(\eta, v) + M(J^{-1}\ddot{\eta}_d + \dot{J}^{-1}\dot{\eta}_d + \alpha(\dot{\eta}_d - \dot{\eta}) + K \tanh(As)) \quad (44)$$

Where K and A are 6×6 diagonal matrices with positive coefficients.

4. Real-Time Experiments and Results

The experimental setup and tested scenarios for evaluating the proposed FTC solution are presented in this section. The results obtained from the experiments are discussed in the following subsection. All of the conducted experiments were video-recorded, and can be visualized in the attached complementary video.

4.1. Experimental setup

A series of validation experiments were performed in a laboratory pool of 1.30m depth (c.f. Fig. 5a) to evaluate the proposed fault-tolerant control allocation method. These experiments include a large grid of size $3m \times 4m$ (cf. Fig 5b). The grid contains 328 ArUco markers Garrido-Jurado, Muñoz-Salinas, Madrid-Cuevas and Marín-Jiménez (2014), 72 of size 0.25m and 216 of size 0.1m. The onboard camera captures images at a frequency of 10Hz, and the detected markers are used to provide the robot with its actual position measurements in the Earth fixed frame R_n .

The shallow depth of the pool restricts the range of motion of some degrees of freedom that can be explored, it also affects the vision-based odometry, as the tags can no longer be detected when going deeper, therefore, the chosen reference trajectory to be tracked was a planar elliptic trajectory. The trajectory was generated using the second degree Ordinary Differential Equation denoted in (45). Using a set of pre-filtered desired set-points $\eta_p = [x_p, y_p, z_p, \psi_p]$, the filter generates continuous desired positions $\eta_d = [x_d, y_d, z_d, \psi_d]$, velocities $\dot{\eta}_d = [\dot{x}_d, \dot{y}_d, \dot{z}_d, \dot{\psi}_d]$ and accelerations $\ddot{\eta}_d = [\ddot{x}_d, \ddot{y}_d, \ddot{z}_d, \ddot{\psi}_d]$.

$$\ddot{\eta}_d + 2\gamma\dot{\eta}_d = \gamma^2(\eta_d - \eta_p) \quad (45)$$

The filter is implemented to guarantee the generation of smooth, continuous, and feasible velocities and accelerations, even in the presence of non-linearity in the desired set-points. A double Euler integration is then performed to get the desired states $\eta_d, \dot{\eta}_d$ and $\ddot{\eta}_d$.

The pre-filtered set-points were then designed to achieve a 2D ellipsoidal-shaped trajectory, whose time-trajectories are expressed as follows:

$$x_p(t) = x_i + L_x(-\cos(\omega_x t) + 1) \quad (46)$$

$$y_p(t) = y_i + L_y \sin(\omega_y t) \quad (47)$$

$$z_p(t) = 0.3 \quad (48)$$

$$\psi_p(t) = \text{atan2}(y_d(t + \zeta) - y_p(t), x_d(t + \zeta) - x_p(t)) \quad (49)$$

Although both of the PID and SM controllers were designed to control the robot in 6 DOFs, the robot at this stage can only be controlled in surge, heave, and yaw DOFs. Sway movement is not efficient with the fins positioned at 30 degrees, and this limitation can be addressed in the future with a better mechanical design that allows a more balanced control between all DOFs. To precisely follow a given 3D trajectory, which is essential for underwater exploration or surveying missions, we control the y position indirectly by adjusting the Line of Sight in the desired yaw ψ_p with a look-ahead parameter ζ Fossen, Breivik and Skjetne (2003). The robot is mechanically stable in roll and pitch by design and thus it is not necessary to control these DOFs.

The parameter γ was tuned manually to guarantee feasible accelerations by the robot in the case where ψ_p changes abruptly because of the non-continuous atan2 function (49). The parameters values for trajectory generation are summarized in Table 3. The offset parameters x_i and y_i are selected based on the measured initial location of the robot, such that the trajectory would start from that point in space.

The following experimental scenarios were evaluated for both the PID and SM controller for the tracking of the above-defined trajectory:

- Scenario 1 (Nominal): All fins are healthy.
- Scenario 2 (RR): The rear right fin is faulty.
- Scenario 3 (RL): The rear left fin is faulty.
- Scenario 4 (FL): The front left fin is faulty.
- Scenario 5 (FR): The front right fin is faulty.

The gains for the PID and SM controllers were determined through a process of iterative testing and adjustment to achieve optimal performance in the nominal case, where all fins are functioning properly. In order to evaluate the robustness of the two controllers, the same set of parameters were used for all other scenarios without further modification. The numerical values of the gains for the PID and SM controllers are reported in Table 4 and Table 5, respectively. The obtained results are presented in the next subsection.

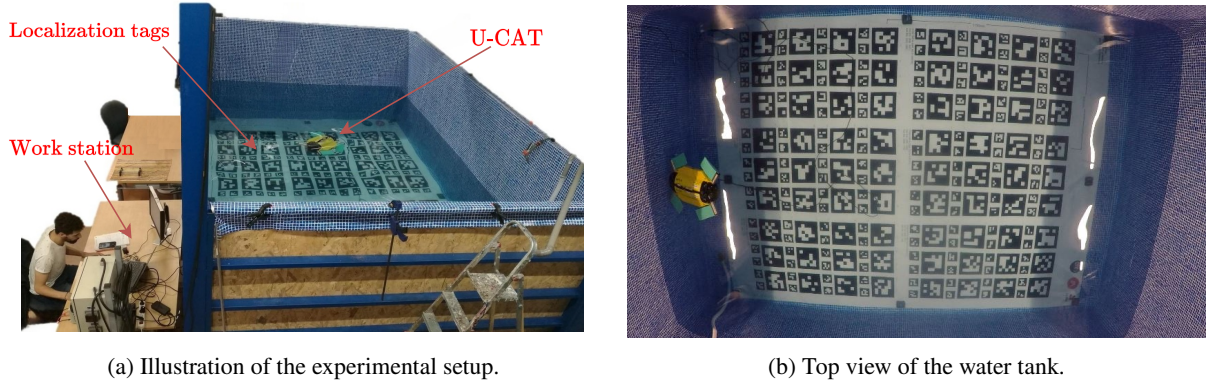


Figure 5: The experimental setup used for real-time experiments at LIRMM laboratory (Montpellier, France).

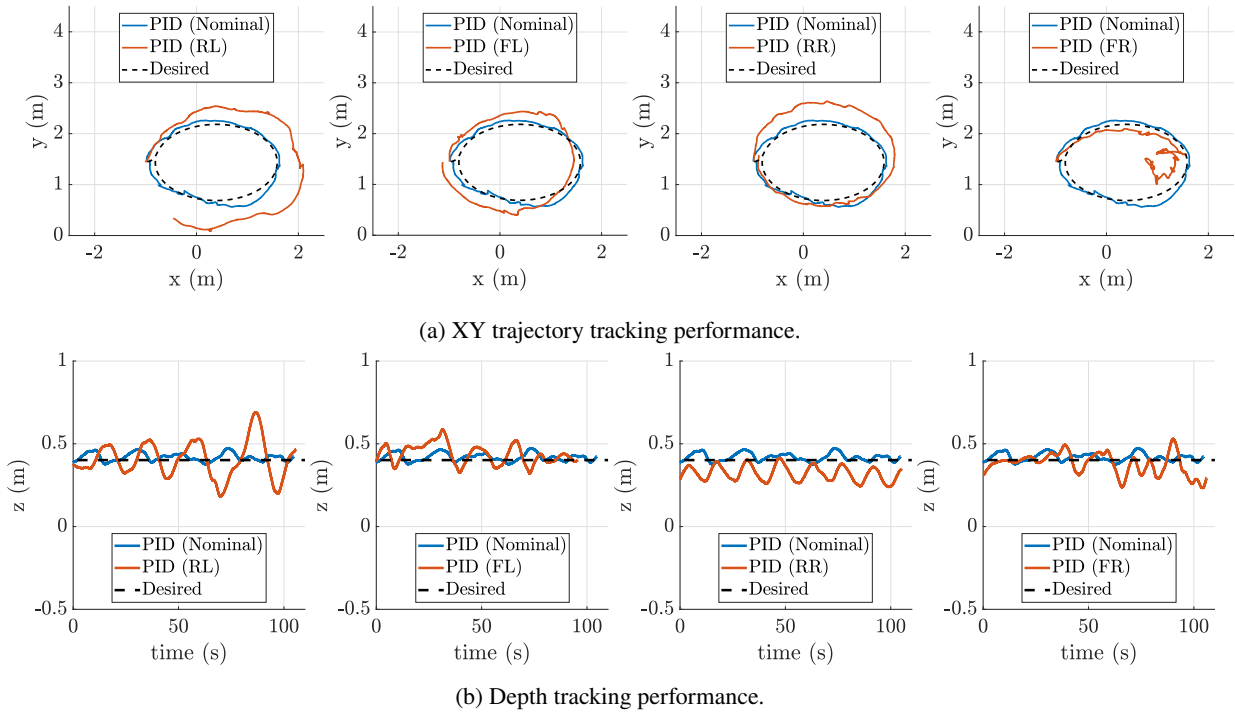


Figure 6: Trajectory tracking results across the different experimental scenarios using the PID controller.

Table 3
Trajectory generation parameters.

L_x	ω_x	L_y	ω_y	ζ	γ
1.2	0.06	0.75	0.06	0.2	5.0

Table 4
The numerical values of the gains for the PID controller.

	K_p	K_d	K_i
Surge	1.15	1.2	0.18
Heave	6.2	1.4	0.7
Yaw	0.35	1.5	0.8

Table 5
The numerical values of the gains for the SMC controller.

	K	α	A
Surge	1.4	0.8	1
Heave	1.3	2.95	1
Yaw	0.9	1.7	1

4.2. Obtained results and discussion

In this section, we present the experimental results obtained from implementing the proposed FTC scheme with PID and SM controllers for the previously described scenarios. The performance of each controller is assessed based on a single complete lap of the elliptical trajectory.

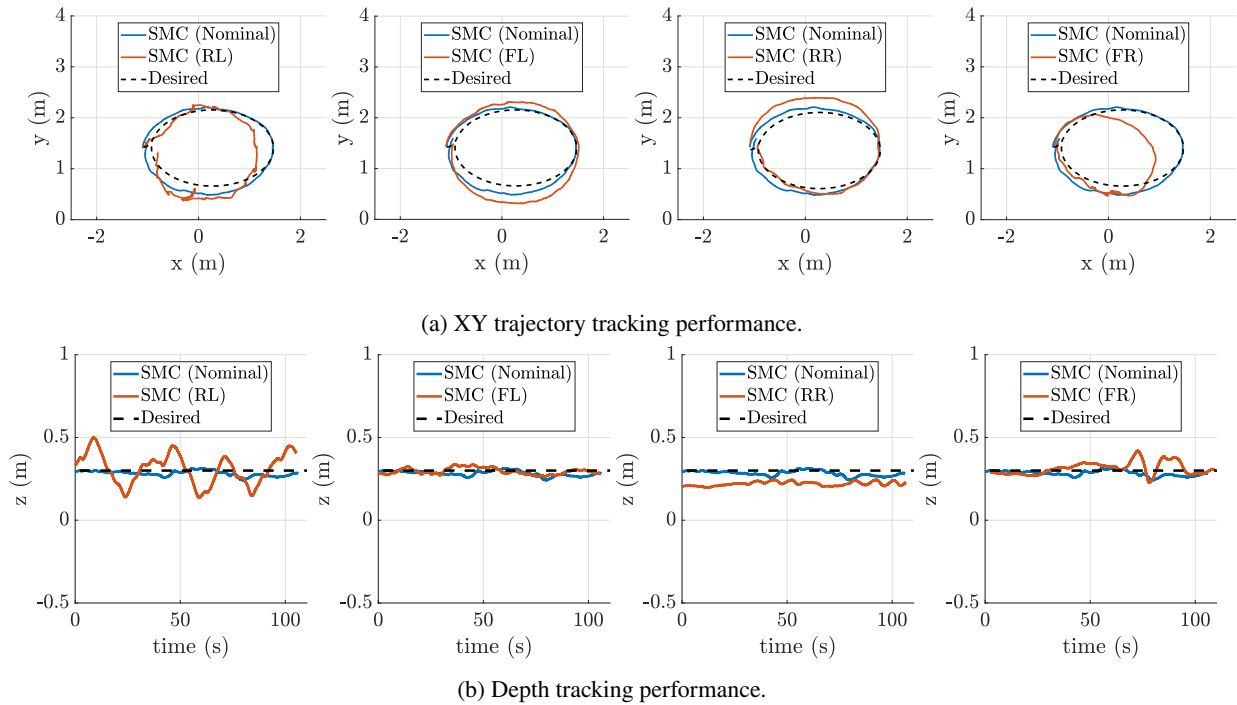


Figure 7: Trajectory tracking results across the different experimental scenarios using the SMC controller.

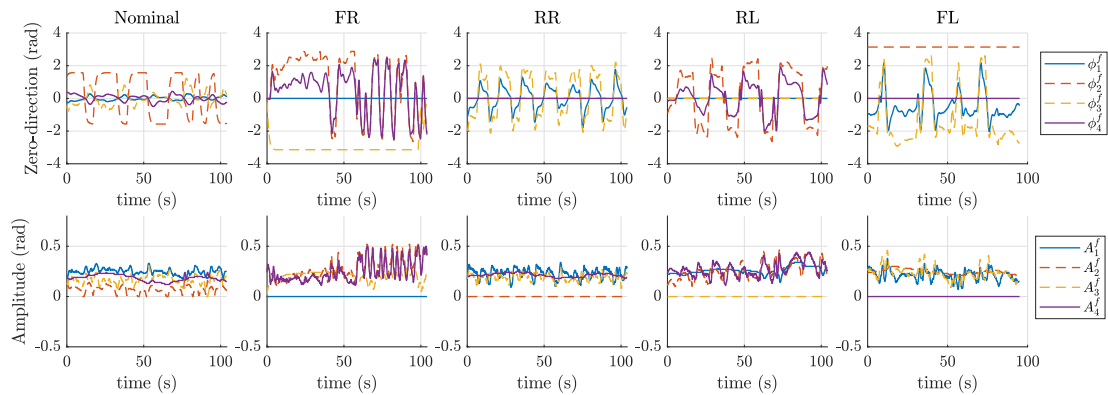


Figure 8: Time-series of the generated zero-direction angles and amplitudes for the different experimental scenarios using the PID controller.

For Scenario 1 (nominal), both the PID and SM controllers enable the robot to accurately track the desired trajectory, as shown in Figures 6 and 7, respectively. The PID controller displays increased oscillations in the zero-direction angle of the rear right fin, which primarily contributes to depth adjustments, as illustrated in Figure 8. In contrast, the SM controller demonstrates reduced oscillation in the zero-direction angle of the rear right fin as shown in 9, resulting in improved tracking performance in terms of root mean square errors (RMS), as displayed in Figure 10. The tracking errors for x and y , reported in Figure 11, reveal that the robot lags slightly behind the reference trajectory when tracking the long side of the ellipse but catches up when tracking the short side.

In Scenario 2 (faulty rear right fin), the tracking performance slightly deteriorates when using the PID controller, as demonstrated in Figure 6. An offset in depth tracking, accompanied by oscillations, results from the robot's positive buoyancy and the fins' inability to generate adequate heave force without switching configuration, as depicted in Figure 8. Conversely, the SM controller facilitates better tracking performance when the rear right fin is faulty, as exhibited in Figure 7. Although depth tracking performance is slightly compromised, overall trajectory tracking remains satisfactory. The fin zero-directions are significantly smoother, as shown in Figure 9.

In Scenario 3 (faulty rear left fin), the tracking performance for all degrees of freedom declines significantly

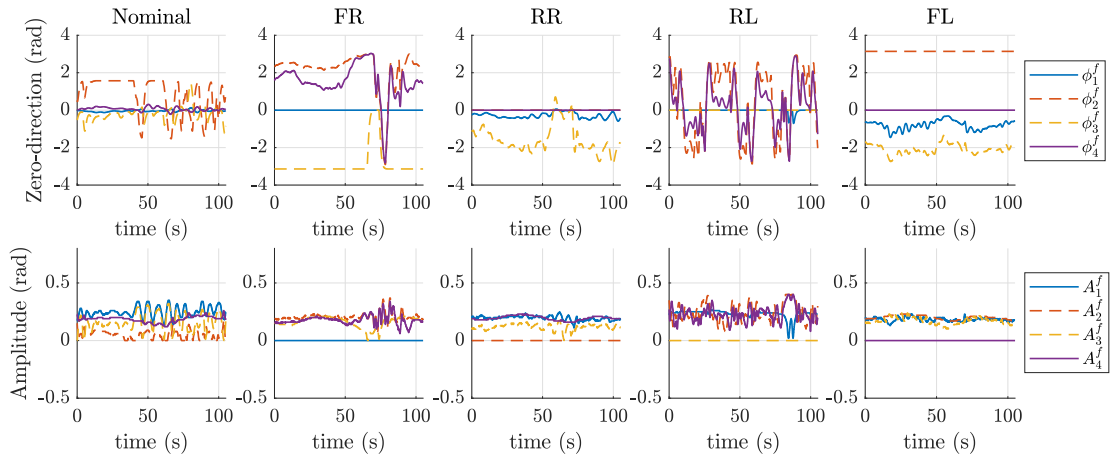


Figure 9: Time-series of the generated zero-direction angles and amplitudes for the different experimental scenarios using the SM controller.

when using the PID controller, as displayed in Figure 6. The rear left fin plays a vital role in adjusting the heading for a clockwise trajectory, and to compensate, the PID generates control inputs that lead to oscillatory behavior in the fins' zero-directions. In contrast, the SM controller offers superior tracking performance, as depicted in Figure 7 and demonstrated in Figure 10. A comparison of the tracking errors for x and y between the two controllers is shown in Figure 11, which clearly highlights the superior performance of the SMC controller.

In Scenario 4 (faulty front left fin), tracking performance is slightly worse compared to the nominal case when using the PID controller, as evidenced in Figure 6. Since the front left fin is primarily responsible for generating surge force, the only DOF affected by its loss is the tracking of x , as shown in Figure 10. Additionally, Figure 8 shows that the rear right fin switches orientation to π to compensate for the required surge force and heading yaw adjustments. The SM controller, however, ensures excellent depth control tracking and accurate overall trajectory tracking, as displayed in Figure 7. The generated zero-directions are considerably smoother, as illustrated in Figure 9, leading to better performance.

In Scenario 5 (faulty front right fin), the PID controller fails to correctly track the reference trajectory, as shown in Figure 6. Since the front right fin plays a significant role in both generating surge force and adjusting the heading for tracking a clockwise trajectory, the remaining fins struggle to properly compensate for this loss with the PID inputs. As illustrated in Figure 8, the fin zero-direction of the front left fin constantly switches signs after the first 50 seconds, which coincides with making a hard turn. On the other hand, the SM controller enables improved tracking performance for all degrees of freedom, as depicted in Figure 7. The importance of the front-right fin for tracking this specific trajectory is also noticeable, although the SM controller handles it better than the PID.

Overall, the proposed FTC scheme with the SM controller provides satisfactory tracking performance in the presence of fin failures. The results demonstrate that the robot can follow the reference trajectory using only the three highly-coupled healthy fins, without the need for adjusting the controller gains.

These results also indicate the effectiveness of the proposed FTC scheme in handling actuation failures, even in the worst-case scenario for tracking the studied reference trajectory. This is particularly important for a symmetrical robot with a symmetrical design, as the worst-case scenario can be deduced based on the type of reference trajectory. This information can be utilized to design high-level controllers that adapt the reference trajectory and bypass worst-case scenarios.

5. Conclusion and Future Works

In conclusion, this paper has addressed the problem of fault-tolerant control for a highly coupled fin-actuated AUV. We have proposed an active fault-tolerant control scheme that utilizes a control allocation switching mechanism to properly allocate controller forces to healthy fins in the event of a fault. The effectiveness of the proposed method was evaluated through experimental studies involving trajectory tracking tasks using two different control laws: PID and sliding mode control. The results indicate that the use of a robust controller, such as sliding mode control, in conjunction with the proposed fault-tolerant control scheme, allows for superior handling of faulty cases compared to conventional PID control.

While the main focus of our work is on the fault-tolerant control allocation strategy, which is independent of specific disturbances such as sea currents, we acknowledge that the influence of sea currents can be an important factor in real-world applications. Although our experiments do not specifically address the impact of external disturbances such as sea currents, our analysis provides insights into the performance

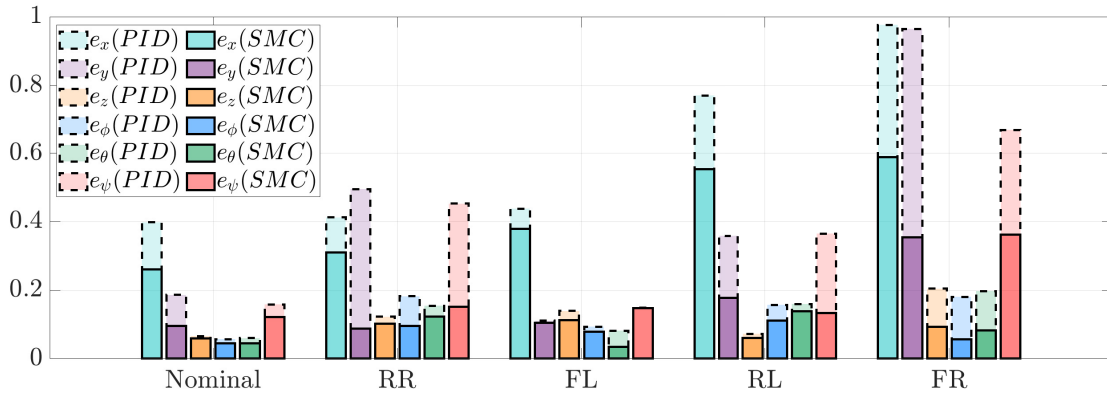


Figure 10: Bar plot of the RMS errors for trajectory tracking of all the studied scenarios. The errors for the position and orientation, expressed in meters and radians, respectively, are reported for a single trial for each case

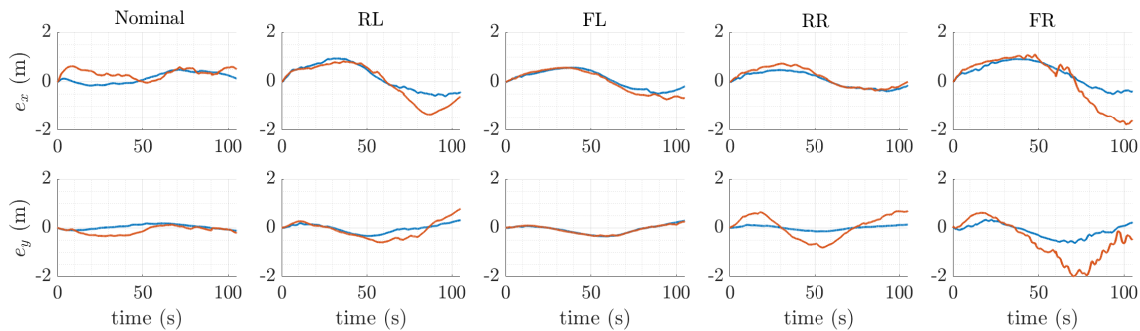


Figure 11: Tracking errors of x and y positions for all the studied scenarios. The errors are depicted for each scenario, illustrating the performance of the control strategies in various fault conditions.

and effectiveness of the proposed control strategy under actuator failure scenarios. As part of future work, we plan to evaluate the performance of the proposed control strategy in environments with sea currents, which will help to further validate the robustness and applicability of our approach.

We also plan to extend the proposed method to more complex cases, allowing for additional degrees of freedom control. This would enable more comprehensive and precise trajectory tracking under demanding conditions. Moreover, we plan to address the challenges associated with handling multiple actuation faults simultaneously, developing adaptive fault-tolerant strategies that can cope with various fault scenarios. This would further enhance the reliability and performance of fin-actuated AUVs, ensuring their safe and efficient operation in the presence of faults.

References

Alwi, H., Edwards, C., 2008. Fault tolerant control using sliding modes with on-line control allocation. *Automatica* 44, 1859–1866.

Antonelli, G., 2003. A survey of fault detection/tolerance strategies for auvs and rovs, in: *Fault diagnosis and fault tolerance for mechatronic systems: Recent advances*. Springer, pp. 109–127.

Baldini, A., Ciabattini, L., Felicetti, R., Ferracuti, F., Monteriù, A., Fasano, A., Freddi, A., 2017. Active fault tolerant control of remotely operated vehicles via control effort redistribution, in: *International Design Engineering Technical Conferences and Computers and Information in*

Engineering Conference, American Society of Mechanical Engineers. p. V009T07A002.

Chemori, A., Kuusmik, K., Salumäe, T., Kruusmaa, M., 2016. Depth control of the biomimetic u-cat turtle-like auv with experiments in real operating conditions, in: *2016 IEEE International Conference on Robotics and Automation (ICRA)*, IEEE. pp. 4750–4755.

Edwards, C., Spurgeon, S., 1998. *Sliding mode control: theory and applications*. Crc Press.

Fossen, T.I., 2011. *Handbook of marine craft hydrodynamics and motion control*. John Wiley & Sons.

Fossen, T.I., Breivik, M., Skjetne, R., 2003. Line-of-sight path following of underactuated marine craft. *IFAC proceedings volumes* 36, 211–216.

Gambhire, S., Kishore, D.R., Londhe, P., Pawar, S., 2021. Review of sliding mode based control techniques for control system applications. *International Journal of Dynamics and Control* 9, 363–378.

Garrido-Jurado, S., Muñoz-Salinas, R., Madrid-Cuevas, F.J., Marín-Jiménez, M.J., 2014. Automatic generation and detection of highly reliable fiducial markers under occlusion. *Pattern Recognition* 47, 2280–2292.

Kadiyam, J., Parashar, A., Mohan, S., Deshmukh, D., 2020. Actuator fault-tolerant control study of an underwater robot with four rotatable thrusters. *Ocean Engineering* 197, 106929.

Kruusmaa, M., Gkliva, R., Tuhtan, J., Tuvikene, A., Alfredsen, J., 2020. Salmon behavioural response to robots in an aquaculture sea cage. *Royal Society open science* 7, 191220.

Liu, F., Tang, H., Qin, Y., Duan, C., Luo, J., Pu, H., 2022a. Review on fault diagnosis of unmanned underwater vehicles. *Ocean Engineering* 243, 110290.

Liu, X., Zhang, M., Liu, X., Zhao, W., 2022b. Finite-time extended state observe based fault tolerant control for autonomous underwater vehicle with unknown thruster fault. *Journal of Marine Science and Engineering*

- 10, 1624.
- Low, K., 2011. Current and future trends of biologically inspired underwater vehicles, in: 2011 Defense Science Research Conference and Expo (DSR), IEEE. pp. 1–8.
- Meurer, C., Simha, A., Kotta, Ü., Kruusmaa, M., 2019. Nonlinear orientation controller for a compliant robotic fish based on asymmetric actuation, in: 2019 International Conference on Robotics and Automation (ICRA), IEEE. pp. 4688–4694.
- Ni, L., 2001. Fault-tolerant control of unmanned underwater vehicles. Ph.D. thesis. Virginia Polytechnic Institute and State University.
- Omerdic, E., Roberts, G., 2004. Thruster fault diagnosis and accommodation for open-frame underwater vehicles. *Control engineering practice* 12, 1575–1598.
- Penrose, R., 1955. A generalized inverse for matrices, in: *Mathematical proceedings of the Cambridge philosophical society*, Cambridge University Press. pp. 406–413.
- Preston, V., Salumäe, T., Kruusmaa, M., 2018. Underwater confined space mapping by resource-constrained autonomous vehicle. *Journal of Field Robotics* 35, 1122–1148.
- RB, A.A., Hemakumar, B., Prasad, M., 2018. Robotic fish locomotion & propulsion in marine environment: A survey, in: 2018 2nd International Conference on Power, Energy and Environment: Towards Smart Technology (ICEPE), IEEE. pp. 1–6.
- Remmas, W., Chemori, A., Kruusmaa, M., 2021a. Diver tracking in open waters: A low-cost approach based on visual and acoustic sensor fusion. *Journal of Field Robotics* 38, 494–508.
- Remmas, W., Chemori, A., Kruusmaa, M., 2021b. Inverse-model intelligent control of fin-actuated underwater robots based on drag force propulsion. *Ocean Engineering* 239, 109883.
- Ren, Z., Wang, T., Wen, L., 2015. Hydrodynamic function of a robotic fish caudal fin: effect of kinematics and flow speed, in: 2015 IEEE/RSJ International Conference on Intelligent Robots and Systems (IROS), IEEE. pp. 3882–3887.
- Salumäe, T., Chemori, A., Kruusmaa, M., 2016. Motion control architecture of a 4-fin u-cat auv using dof prioritization, in: 2016 IEEE/RSJ International Conference on Intelligent Robots and Systems (IROS), IEEE. pp. 1321–1327.
- Salumäe, T., Raag, R., Rebane, J., Ernits, A., Toming, G., Ratas, M., Kruusmaa, M., 2014. Design principle of a biomimetic underwater robot u-cat, in: 2014 Oceans-St. John's, IEEE. pp. 1–5.
- Salumäe, T., Chemori, A., Kruusmaa, M., 2019. Motion control of a hovering biomimetic four-fin underwater robot. *IEEE Journal of Oceanic Engineering* 44, 54–71. doi:10.1109/JOE.2017.2774318.
- Samy, I., Postlethwaite, I., Gu, D.W., 2011. Survey and application of sensor fault detection and isolation schemes. *Control Engineering Practice* 19, 658–674.
- Sarkar, N., Podder, T.K., Antonelli, G., 2002. Fault-accommodating thruster force allocation of an auv considering thruster redundancy and saturation. *IEEE Transactions on Robotics and Automation* 18, 223–233.
- Scaradozzi, D., Palmieri, G., Costa, D., Pinelli, A., 2017. Bcf swimming locomotion for autonomous underwater robots: a review and a novel solution to improve control and efficiency. *Ocean Engineering* 130, 437–453.
- Slotine, J.J.E., Li, W., et al., 1991. *Applied nonlinear control*. volume 199. Prentice hall Englewood Cliffs, NJ.
- Utkin, V.I., 2013. *Sliding modes in control and optimization*. Springer Science & Business Media.
- Wang, Y., Wilson, P.A., Liu, X., et al., 2015. Adaptive neural network-based backstepping fault tolerant control for underwater vehicles with thruster fault. *Ocean Engineering* 110, 15–24.
- Weymouth, G.D., 2016. Biologically inspired force enhancement for maritime propulsion and maneuvering. arXiv preprint arXiv:1609.06559.
- Xie, O., Zhu, Q., Shen, L., Ren, K., 2018. Kinematic study on a self-propelled bionic underwater robot with undulation and jet propulsion modes. *Robotica* 36, 1613–1626.
- Yang, K.C., Yuh, J., Choi, S.K., 1998. Experimental study of fault-tolerant system design for underwater robots, in: *Proceedings*. 1998 IEEE International Conference on Robotics and Automation (Cat. No. 98CH36146), IEEE. pp. 1051–1056.
- Yang, Y., Wang, J., Wu, Z., Yu, J., 2018. Fault-tolerant control of a cpg-governed robotic fish. *Engineering* 4, 861–868.
- Yu, J., Wang, L., 2005. Parameter optimization of simplified propulsive model for biomimetic robot fish, in: *Proceedings of the 2005 IEEE International Conference on Robotics and Automation*, IEEE. pp. 3306–3311.